Available online at www.sciencedirect.com

SciVerse ScienceDirect

Acta Materialia 60 (2012) 6301–6311

Acta MATERIALIA

www.elsevier.com/locate/actamat

Atomistic characterization of pseudoelasticity and shape memory in NiTi nanopillars

Yuan Zhong, Ken Gall, Ting Zhu *

Woodruff School of Mechanical Engineering, Georgia Institute of Technology, Atlanta, GA 30332, USA

Received 22 May 2012; received in revised form 4 August 2012; accepted 6 August 2012
Available online 13 September 2012

Abstract

Molecular dynamics simulations are performed to study the atomistic mechanisms governing the pseudoelasticity and shape memory in nickel–titanium (NiTi) nanostructures. For a ⟨1 1 0⟩ – oriented nanopillar subjected to compressive loading–unloading, we observe either a pseudoelastic or shape memory response, depending on the applied strain and temperature that control the reversibility of phase transformation and deformation twinning. We show that irreversible twinning arises owing to the dislocation pinning of twin boundaries, while hierarchically twinned microstructures facilitate the reversible twinning. The nanoscale size effects are manifested as the load serration, stress plateau and large hysteresis loop in stress–strain curves that result from the high stresses required to drive the nucleation-controlled phase transformation and deformation twinning in nanosized volumes. Our results underscore the importance of atomistically resolved modeling for understanding the phase and deformation reversibilities that dictate the pseudoelasticity and shape memory behavior in nanostructured shape memory alloys.

Keywords: Shape memory alloy; Pseudoelasticity; Nanopillar; Molecular dynamics; Phase transformation

1. Introduction

Shape-memory alloys (SMAs), when deformed at a low temperature, recover to their original shape upon unloading and heating [1–3]. Nickel–titanium (NiTi) is one of the most widely used SMA [4]. The shape memory effect of NiTi usually results from the reversible martensitic phase transformation between the cubic B2 (austenite) and monoclinic B19′ (martensite) phases. NiTi can also exhibit pseudoelasticity [4], i.e. deformation is fully recovered upon unloading without the aid of heating. Compared to shape memory, pseudoelasticity similarly involves the martensitic phase transformation, but it occurs when the deformation temperature is higher, typically above the austenite finish temperature A_f.

Both pseudoelasticity and shape memory have been extensively studied in bulk SMAs [1–3]. However, these unique properties and size effects remain largely unexplored in nanoscale SMAs [5], while they are being increasingly considered for use in micro/nanodevices for sensing, actuation, shape memory and mechanical damping [6,7]. Recent development in nanomechanical testing provides opportunities for illuminating the nanometer length scale effects on SMAs [8–21]. For example, Frick et al. showed that decreasing the diameter of NiTi nanopillars inhibits the pseudoelastic behavior and ultimately suppresses it for diameters of less than 200 nm [11]. This size effect could be possibly attributed to the suppression of martensitic phase transformation in small samples, so favoring the irreversible deformation mechanism of dislocation plasticity. However, in a recent in situ electron diffraction experiment, the martensitic phase transformation of B2 → B19′ was observed in NiTi pillars of 200 nm diameter [15]. It was thus suggested that the loss of pseudoelasticity arises owing to incomplete strain recovery, despite the occurrence of martensitic phase transformation [16]. In contrast to loss of pseudoelasticity, the

* Corresponding author.
E-mail address: ting.zhu@me.gatech.edu (T. Zhu).

1359-6454/$36.00
http://dx.doi.org/10.1016/j.actamat.2012.08.004

shape memory was measured for pillars with diameters of 200 nm [16].

To understand the length scale effects on nanostructured SMAs, it is highly desired to develop the physics-based models to explore the structure–property relationship in these systems [22–32]. To this end, here we report an atomistic study of the pseudoelasticity and shape memory behaviors in NiTi nanopillars by using molecular dynamics (MD) simulations. We focus on the stress-induced martensitic phase transformation and deformation twinning, while temperature-driven phase transformations have been reported in a recent publication [28]. It is important to note that, compared to the previous atomistic study of pseudoelasticity and shape memory in pure metals [33–36], the NiTi alloy is complicated with the formation and evolution of a variety of phases (e.g. B2, B19, B19′, R and base centered orthorhombic (BCO)) and twin structures (e.g. type I, type II and compound twins) [4]. However, it is likely that the facile multi-phase and multi-twin features could produce the pseudoelasticity and shape memory effects that are more robust and thus highly desirable to the "smart" micro/nanodevices. In this work, by controlling the applied strains and temperatures, we have simulated various characteristic stress–strain behaviors in shape memory alloys, such as pseudoelastic deformation, loss of pseudoelasticity and shape memory. Our detailed atomistic characterization of the phase transformation and deformation twinning products offers new insights into the physical mechanisms governing the thermomechanical behavior of NiTi nanostructures.

2. Method

A Finnis–Sinclair-type many-body interatomic potential [37] is used to describe the NiTi system. This potential was originally developed by Lai and Liu [22], but it suffered from discontinuities at the cutoff radius. We modified the potential function by smooth interpolations near the cutoff with cubic polynomials [28]. The resulting NiTi potential not only enabled well-behaved molecular statics and dynamics simulations, but also improved the predicted properties, including lattice constant and cohesive energy for a variety of phases, as compared with ab initio calculations in Table II in our recent publication [28].

In this work, we perform the MD simulations of uniaxial compression of NiTi nanopillars by using LAMMPS [38]. The initial structure is the ordered B2 phase. In Section 3.1, a nanopillar with 46,080 atoms is constructed. It is 25.6 nm long, with a nearly square cross-section, 4.8 nm × 5.1 nm. The periodic boundary condition is applied only in the axial direction, such that the sidewalls of nanopillars are traction-free. The axial direction of the nanopillar is aligned with $\langle 1\,1\,0\rangle_{B2}$ [13]. By thermal equilibration, the simulation temperature is set to 400 K, ~50 K higher than A_f (~350 K, to be discussed at the end of this section). The system is relaxed at zero stresses for 200,000 MD time steps, each of which is 0.5 fs. The uniaxial compression is then applied by strain control. To explore the pseudoelastic deformation, a limited load range is applied up to 6.6% engineering strain. Note that all the strain values given in this paper refer to the magnitude of the applied compressive strain. The aforementioned strain limit is achieved in 400,000 time steps, followed by unloading to zero strain in another 400,000 time steps. As such, both loading and unloading correspond to a constant strain rate of $\sim 3 \times 10^8\ s^{-1}$. In Section 3.2, we study the irreversible deformation after the complete martensitic phase transformation by imposing a larger compressive strain up to 10.6%. In Section 3.3, the temperature effect is investigated on both phase transformation and deformation twinning by reducing the deformation temperature to 350 K, close to A_f. In Section 3.4, the size effects on the stress- and temperature-driven phase transformation are discussed, as compared with the bulk NiTi behavior.

In all the MD simulations, we identify the formation of new phases in terms of the transformed lattice constants, internal atomic shuffling and particularly monoclinic angle γ, i.e. $\gamma = 90°$ for B2 and B19, $\gamma = 98°$ for B19′, and $\gamma = 108°$ for the BCO phase [28]. To reduce the error from thermal fluctuations, the aforementioned geometrical parameters are calculated by averaging over tens of MD time steps. Note that for a given temperature, several MD simulations have been performed with different initial distributions of randomly assigned atomic velocities, in order to explore the possibly different products of phase transformation and deformation twinning.

To facilitate the analysis of crystallography and twin geometry, Fig. 1 shows the lattice structure of the B2 phase with both cubic and tetragonal unit cells. We use a_0 to represent the lattice constant of the cubic unit cell. Correspondingly, the lattice parameters of the tetragonal cell are given by $a = a_0$ and $b = c = \sqrt{2}a_0$. In this paper, all the crystallographic orientations of different phases are

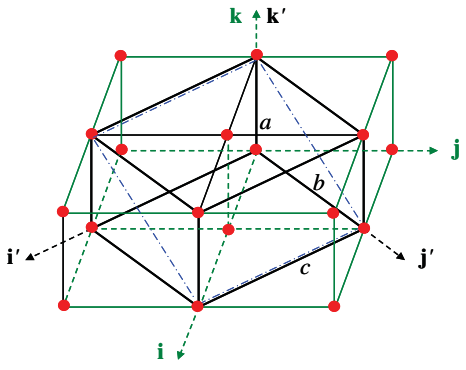

Fig. 1. Schematic of a tetragonal unit cell (black lines) and four cubic unit cells (green lines) in the untransformed B2 phase. Only Ti atoms (red circles) are shown for clarity. The orthonormal vectors $(\mathbf{i},\mathbf{j},\mathbf{k})$ are along the cube axes, and the orthonormal vectors $(\mathbf{i}',\mathbf{j}',\mathbf{k}')$ are along the cube directions of $[1\,\bar{1}\,0]$, $[1\,1\,0]$ and $[0\,0\,1]$, respectively. The rectangle enclosed by dash-dotted lines is the twin plane, refereed to the basis of the cubic unit cell. (For interpretation of the references to color in this figure legend, the reader is referred to the web version of this article.)

referred to the $(\mathbf{i},\mathbf{j},\mathbf{k})$ basis of the cubic cell of the parent B2 phase. The martensitic transformation of B2 → B19′ takes a tetragonal unit cell into a monoclinic cell. The associated lattice deformation involves the expansion and contraction of the tetragonal cell, as well as a simple shear. In our notation, $a < b < c$. In B19′ the monoclinic angle γ between edges with length of a and c is $\sim 98°$, as measured from experiments [4] and predicted from our MD simulations. The martensitic transformation also involves the atomic shuffling in unit cells, which can be directly simulated by MD.

As a reference to the present MD study of the thermomechanical behavior of nanopillars, we briefly review the phase transformation properties of bulk NiTi, which have been predicted by the same interatomic potential in our recent publication [28]. In that work, the temperature-driven phase transformation at zero stresses was studied by MD. The simulation began with the B19′ phase in a supercell containing 1152 atoms. The system was subjected to periodic boundary conditions. It was heated from 100 K to 450 K, then cooled down to 100 K. We defined an order parameter W as the overall shear of the supercell, normalized by its maximum value. Fig. 2 shows the time-averaged values of W as a function of temperature. The phase transformation temperatures were estimated by the abrupt change of W, signifying the phase transformation between B19′ (martensite) and B2 (austenite). As shown in Fig. 2, both the austenite start temperature A_s and finish temperature A_f are ~350 K, while the martensite start temperature M_s is ~310 K and the finish temperature M_f is ~290 K. These are reasonably close to the experimental values [28]. Our further MD studies indicated that the size of the periodic supercells does not markedly affect the predicted phase transition temperatures of the bulk NiTi.

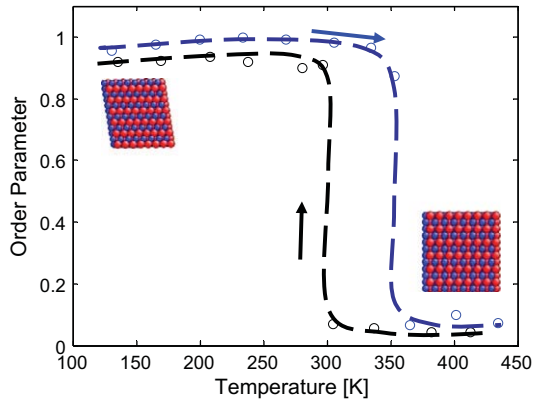

Fig. 2. Temperature-driven, first-order phase transition in bulk NiTi, showing the order parameter W as a function of temperature [28]. Circles are the time-averaged MD results, and dashed lines are the fitting curves, corresponding to the heating (blue line) and subsequent cooling (black line). Insets show the atomic structure of the cubic B2 (lower-right) and monoclinic B19′ (upper-left) phase, respectively, where the blue atoms are Ni and red atoms Ti. (For interpretation of the references to color in this figure legend, the reader is referred to the web version of this article.)

3. Results and discussion

3.1. Pseudoelasticity and reversible phase transformation

Fig. 3 shows the MD results of uniaxial compression of a NiTi nanopillar at a temperature of 400 K, ~50 K above the bulk value of A_f. Fig. 3a presents the initial structure of the nanopillar in the B2 phase. During compression, the successive phase transformations of B2 → B19 → B19′ occur. Fig. 3b plots the corresponding stress–strain curve with the maximum compressive strain of $\varepsilon = 6.6\%$. The compressive deformation constitutes four stages: (I) the initial linear response ($\varepsilon < 2.5\%$) represents the elastic deformation of the B2 (austenite) phase; (II) the continuous but nonlinear response ($2.5\% < \varepsilon < 3\%$) corresponds to the martensitic phase transform of B2 → B19, manifested by a smooth increase of slope; (III) another linear response $3\% < \varepsilon < 5.8\%$) signifies the completion of martensitic phase transformation to B19 and subsequent elastic deformation of B19; (IV) the load drop at $\varepsilon \sim 5.8\%$ indicates the phase transformation of B19 → B19′.

Next, each of the aforementioned loading stages is described in detail. During stage I ($\varepsilon < 2.5\%$), we start with the cubic B2 (CsCl type) phase of NiTi. Fig. 3c shows the schematic of its atomic structure in a conventional tetragonal unit cell which includes both Ni and Ti atoms. This austenite phase is stable at 400 K. Its effective Young's modulus E' is ~29 GPa, estimated from the slope of the initial stress–strain curve in Fig. 3b. Since the nanopillar is compressed in the $\langle 1\,1\,0\rangle_{B2}$ direction, the corresponding Young's modulus can be related to the elastic constants of the B2 phase by

$$E' = \frac{2}{1/C_{44} + 1/(C_{11} + C_{12} - 2C_{12}C_{12}/C_{11})} \tag{1}$$

Using Eq. (1), one can compare E' predicted from our MD with the experimental value. The elastic constants of the B2 phase have been measured by Brill et al. [39] at the same temperature of 400 K as MD. On the basis of their experimental data, we estimate $E' = 39$ GPa, consistent with our MD result. On the other hand, the B2 phase at low temperatures is metastable. It can be accessed in the well-controlled atomistic modeling, but not in experiment. As such, for the 0 K case, we compare the results between the interatomic potential and ab initio density functional theory calculations. Using Eq. (1), we calculate E' from the 0 K elastic constants predicted by the interatomic potential, yielding 72.9 GPa. It is comparable to the value of 62.2 GPa from the ab initio 0 K elastic constants by Hatcher et al. [26], but smaller than 128.7 GPa from Wagner and Windl [24]. From the above results at 400 K and 0 K, one can see a strong temperature effect on the moduli of the B2 phase.

During stage II ($2.5\% < \varepsilon < 3\%$), the stress–strain curve in Fig. 3b is continuous but nonlinear. This stage of deformation features the phase transformation of cubic B2 → orthorhombic B19, as schematically illustrated by

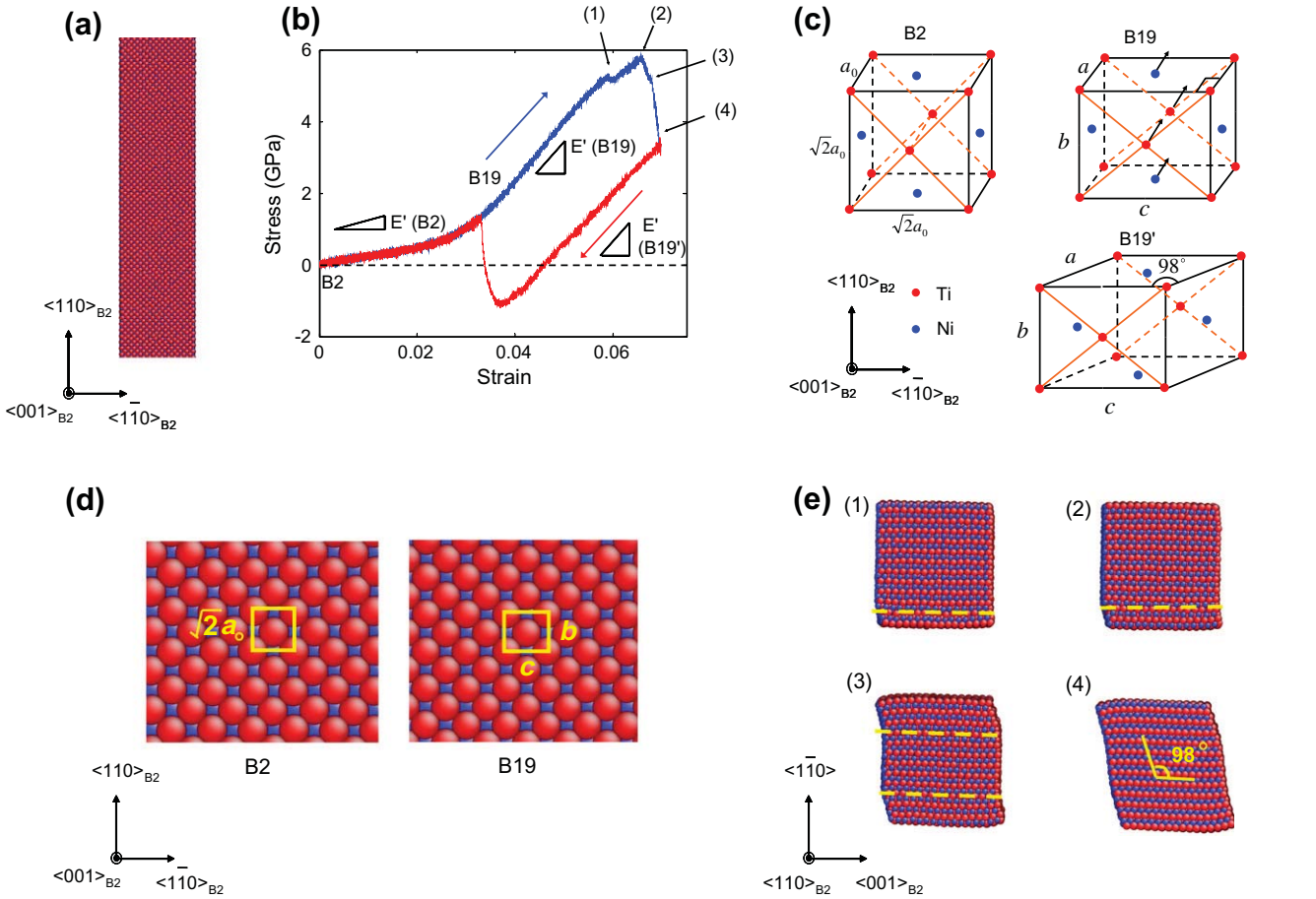

Fig. 3. Nanopillar compression at 400 K with the applied strain up to 6.6%. (a) Initial structure in the ordered B2 phase (red atoms represent Ti and blue atoms Ni). (b) Stress–strain curve of loading (blue) and unloading (red); a positive stress means tension. (c) Schematics of B2, B19, B19′ unit cells. (d) Side view of the nanopillar before and after the phase transformation of B2 → B19. (e) Top view of the sequential steps of the B19 → B19′ phase transformation; the dashed line indicates the phase boundary. (For interpretation of the references to color in this figure legend, the reader is referred to the web version of this article.)

their respective unit cells in Fig. 3c. Fig. 3d shows the atomic structures of nanopillars before and after B2 → B19. The lattice deformation associated with phase transformation can be understood in terms of a direct loading effect. The lattice constant b in B19 is smaller than the corresponding value of $\sqrt{2}a_0$ in B2 [23–25,27]. As a result, the applied compression along $\langle 1\,1\,0\rangle_{B2}$ tends to promote the formation of B19 with a smaller lattice constant in the loading direction. In addition, internal atomic shuffling within the unit cell is observed in our MD, i.e. atoms in $\{1\,1\,0\}$ planes move in the $[0\,0\,1]$ direction, as indicated by arrows in Fig. 3c. Our results agree well with a recent study by Hatcher et al. [25,26]. They performed the first principles calculations of energy barriers of multilayer shear, and found the shuffling on $[0\,0\,1]\{1\,1\,0\}$ requires the lowest energy barrier or even no energy barrier, depending on the number of the sheared layers. The shuffling mode from our MD essentially corresponds to their two-layer $[0\,0\,1]\{1\,1\,0\}$ shuffling. However, this mode is different from the $[1\,\bar{1}\,0]\{1\,1\,0\}$ basal shear/shuffle proposed by Otsuka and Ren [40]. It is still an open question which shuffling mode dominates in the B2 → B19 phase transformation.

During stage III ($3\% < \varepsilon < 5.8\%$), the B19 phase is elastically deformed, and its effective Young's modulus is ~145 GPa. The corresponding experimental data are currently unavailable. Combining stages I–III, we notice that during the B2 → B19 phase transformation, a 5.8% strain can be achieved through a small phase transformation strain only of 0.5% and a large elastic strain of 5.3%. This is because initiation of such a stress-driven transformation process requires a high load (~2.5% elastic strain), which can be sustained by the parent B2 phase as it is single crystalline without pre-existing internal defects. Furthermore, the B2 → B19 phase transformation involves a continuous variation of lattice constant. This implies a gradual diminishing of the energy barrier of the B2 → B19 transformation with increasing load, characteristic of the second-order phase transition. Such a continuous process results in a small transformation strain of 0.5%. The transformation product of the B19 phase can also sustain large elastic strain, as it does not contain pre-existing internal defects either.

During stage IV ($\varepsilon > 5.8\%$), the deformation features the phase transformation of B19 → B19′. The resulting monoclinic angle γ of the B19′ phase is ~98°, as indicated in

Fig. 3c. Note that the shear transformation occurs in the plane (containing a and c) perpendicular to the loading direction. Furthermore, the transformation involves the nucleation and growth of the B19′ phase from the B19 parent matrix, as will be discussed next. The associated stress–strain curve is plotted in Fig. 3b. During this stage of phase transformation, there are two load drops occurring at strains of 5.9% and 6.6%, respectively. The first load drop is relatively small, of only a few hundred megapascals, and is followed by a load increase. The second load drop is considerably larger, at ~2 GPa. The compressive loading terminates at this point, while the stress–strain behavior under a further load increase will be studied to explore the martensite plasticity in the next section.

The aforementioned nucleation and growth of the B19′ phase are shown in detail by a cross-sectional view of the nanopillar in Fig. 3e. The B19′ phase first nucleates at a $\{1\bar{1}0\}_{B2}$ free surface of the pillar (Fig. 3e1), resulting in the first load drop in Fig. 3b. As shown in Fig. 3e2, the B19′ phase grows by migration of a phase boundary (dashed line) with increasing load. When ε reaches ~6.6%, a B19′ phase also nucleates at the opposite $\{1\bar{1}0\}_{B2}$ free surface, Fig. 3e3, and it grows similarly by migration of a phase boundary. Instability occurs when the two phase boundaries are sufficiently close, producing the second load drop and the final product of a uniform B19′ phase, shown in Fig. 3e4. The monoclinic angle γ is 98° in the central region of the pillar, while γ increases notably to 109° near the outer boundaries of the cross-section due to the free surface effect.

The unloading starts with the B19′ phase. Fig. 3b plots the associated stress–strain curve (in red). It comprises two linear parts, with an abrupt stress change in between. The Young's modulus of the initial linear unloading is ~142 GPa, close to the 134 ± 4 GPa measured from experiments at room temperature [41]. At $\varepsilon \approx 3.5\%$, the B19′ phase reverts to B19 and finally to B2, causing a sudden change of stress. This is followed by another linear unloading, with the associated stress–strain curve overlapping the initial loading one (in blue). When the axial strain is reduced to zero, the stress also becomes zero. Clearly, both the phase and load recoveries indicate that the nanopillar undergoes the pseudoelastic deformation during a loading–unloading cycle. In the experiment of NiTi nanopillars, Frick et al. reported that decreasing diameter inhibits the pseudoelastic behavior and ultimately suppresses it for diameters of less than 200 nm [11]. As discussed earlier in Section 1, this size effect has been ascribed to the suppression of martensitic phase transformation or the incomplete reverse martensitic transformation. Nevertheless, our pseudoelastic results do not conflict with their findings. This is because in our strain-controlled MD simulations, the realization of pseudoelasticity, through the B19′ → B2 phase transformation during unloading, actually requires the negative compressive (i.e. tensile) stress that has not been generally imposed in experiments of nanopillar compression [11]. If the unloading was stopped at zero stresses, as in experiment, the phase transformation would not be fully reversible, since the final product would be the B19′ martensite instead of the B2 austenite. Lastly, it is important to emphasize that the chemical effect, i.e. the formation of surface oxides, could play an important role in the loss of pseudoelasticity in the experimentally studied NiTi nanopillars. NiTi alloys can be spontaneously covered by a thin film of $TiO_2 + TiO_x$ with thickness typically in the range of a few tens of nanometers [42,43]. Juan et al. [44] pointed out that such oxides in NiTi nanopillars will exhibit high modulus and compressive strength, thus acting as a stiff outer tube to enclose the NiTi inner core. As a result, much higher loads would need to be applied to deform the nanopillar, achieving the stress for plastic deformation of the NiTi core and potentially suppressing the pseudoelastic behavior, and in particular pseudoelastic recovery. In the future, it would be highly desired to study the influence of surface oxides in NiTi nanopillars by atomistic modeling, but it is beyond the scope of this work as the Ni–Ti–O interatomic potential is currently not available.

3.2. Irreversible twinning and loss of pseudoelasticity

To study the irreversible deformation in NiTi martensite, we apply a larger range of compressive strain up to 10.6%. The corresponding stress–strain curve is shown in Fig. 4a, where the loading regime between points (I) and (II) represents the successive phase transformation of B2 → B19 → B19′, as described in detail in Section 3.1. In this section we focus on the subsequent deformation behavior. Upon continual compression, the B19′ phase at point (II) is not stable, and it immediately transforms to the BCO phase [23] without an obvious change in the stress–strain curve. Fig. 4b shows the cross-sectional view of the nanopillar with the BCO phase. One major difference between the BCO and B19′ phase is the monoclinic angle γ, i.e. 108° in BCO vs. 98° in B19′ as schematically indicated in Fig. 4c and Fig. 3c, respectively. It should be emphasized that γ in BCO cannot be an arbitrary value, because the orthorhombic structure dictates $\gamma = \arcsin(a/2c)$, as illustrated in Fig. 4d [23]. Incidentally, the ab initio calculations show that the BCO phase in NiTi is the ground state under zero stresses at 0 K, with its energy lower than that of B19′, the commonly observed martensitic phase in experiments [23,24,26]. Note that the formation of the BCO phase in our MD simulations is driven by the applied mechanical loading at finite temperature.

Deformation twinning occurs when the applied compressive strain reaches ~8.5%, causing a sharp load drop from 5 GPa to 0.6 GPa, i.e. from points (III) to (IV) in Fig. 4a. Fig. 4e shows the nucleation and growth of a twinned shear band in the martensitic BCO phase. Our analysis of the crystallography and structure changes indicates that the twin plane is $\{1\,1\,2\}_{B2}$, as highlighted by the shaded plane in a BCO unit cell in Fig. 4c as well as the plane enclosed by the blue dashed lines in Fig. 1. The direction of twin shear does not appear to coincide with any

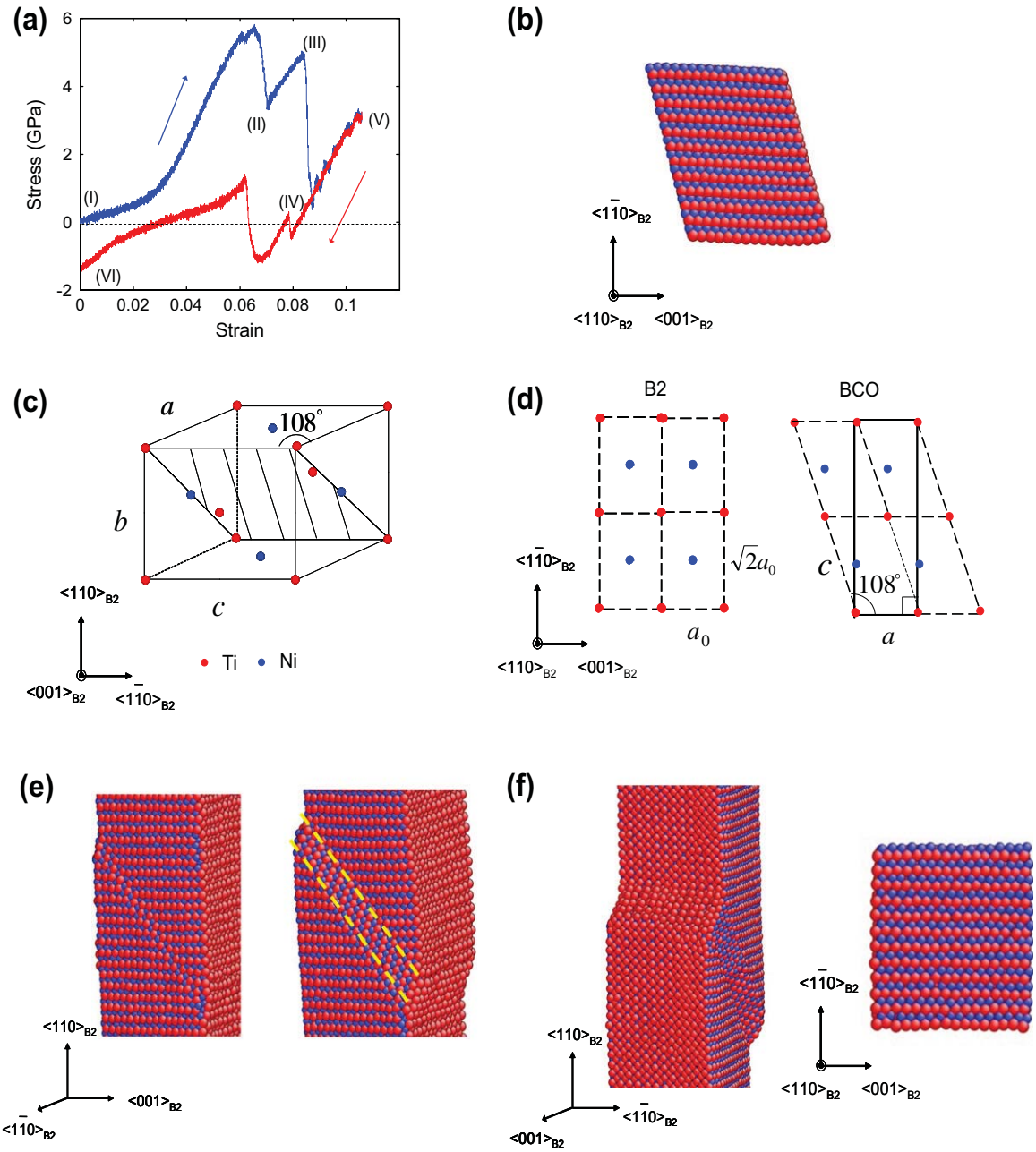

Fig. 4. Nanopillar compression at 400 K with the applied strain up to 10.6%. (a) Stress–strain curve of loading (blue) and unloading (red). (b) Cross-sectional view of nanopillar, showing the martensitic BCO phase. (c) Schematic of a BCO unit cell. (d) Two-dimensional projection of B2 and BCO unit cells, showing the uniquely defined monoclinic angle $\lambda = \arcsin(a/2c) = 108°$ in BCO unit cells. (e) Compressed nanopillar in the BCO phase, showing the formation (left) and growth (right) of a twinned shear band in between dashed lines. (f) Nanopillar after unloading to zero strain, showing the residual twinned shear band (left) and the cross-sectional view of the B2 phase (right). (For interpretation of the references to color in this figure legend, the reader is referred to the web version of this article.)

typical crystallographic orientation. Such shear transformation is considered as type I twinning.

Next, we fully unload the sample to zero strain. The unloading stress–strain curve is shown in Fig. 4a (in red). Compared to Fig. 3b, an abrupt load change similarly occurs due to the phase transformation of BCO → B2. However, a major difference is the residual tensile stress of ~1.4 GPa left in the nanopillar at zero strain, indicating a loss of pseudoelasticity. As shown in Fig. 4f, the initial B2 phase has been recovered after unloading, but the twinned shear band remains in the final product. It is interesting to note that during the loading–unloading cycle, the system undergoes a series of B2 → B19 → B19′ → BCO → B2 phase transformations that finally recover the initial B2 austenite. However, the deformation twin is irreversible, leading to a loss of pseudoelasticity.

The above irreversibility of deformation twinning can be attributed to the dislocation pinning effect on twin

boundaries. Twins in the B19′ phase are usually reversible in bulk NiTi, as shown in MD simulations of the temperature-driven phase transformation at zero stresses [28]. However, the above deformation twinning in BCO is irreversible and could be caused by the nucleation of dislocations. In the final product containing an irreversible twin shear band, we observed residual dislocations in the $\{1\,1\,2\}_{B2}$ slip plane. This implies that during unloading, those dislocations could act as pinning defects in twin boundaries, preventing the de-twinning process. The irreversible twinning could be further related to the delayed formation of deformation twins in de-confined nanopillars. Namely, the lack of confinement on nanopillars (with the traction-free sidewalls) does not necessarily require the formation of twins at low loads, and the phase transformation to BCO occurs favorably to release the accumulated strain energy with increasing deformation instead. It follows that the deformation twinning is postponed to a late stage of loading when the applied stress is considerably high (~5 GPa). As a result, the high stress could trigger both twinning shear and dislocation nucleation concomitantly. Upon further unloading, the reverse load cannot eliminate these dislocations that act as pinning defects to impede the motion of twin boundaries, thus causing the irreversibility at 400 K. Finally, we note that the above MD results are qualitatively similar with different initial distributions of randomly assigned atomic velocities.

3.3. Temperature effect and reversible twinning

To study the temperature effect on phase transformation and deformation twinning in NiTi nanopillars, we lower the deformation temperature from 400 K, as studied in Sections 3.1 and 3.2, to 350 K, close to A_f. MD simulations are performed with various initial conditions of randomly generated atomic velocity distribution, yielding different final products. This implies that the thermomechanical response of NiTi nanostructures near the phase transformation temperature could become less deterministic than that at high temperatures. During loading, all the nanopillars undergo the phase transformations of B2 → B19 → BCO at 350 K, in contrast to B2 → B19 → B19′ → BCO at 400 K. In addition to phase transformations, two different kinds of twin microstructures, i.e. type I twin and "twins within twin", form in the nanopillars when further loaded at 350 K. Similar to results in Section 3.2, the type I twin is irreversible due to the nucleated dislocations that pin the twin boundaries, and it is not further discussed for brevity. Here we focus on the newly observed "twins within twin", which are fully recoverable after unloading. As a result, both shape memory and pseudoelastic behaviors can be observed.

Fig. 5 shows an MD result at 350 K, exhibiting the reversible twins within twin and shape memory effect. Starting with the B2 phase, the transformation to B19 occurs at the strain of 0.7%, much smaller than the corresponding strain of 2.5% at 400 K. This difference is understandable, because the low temperature encourages formation of the martensite. As the compressive strain reaches 4%, a direct transformation of B19 → BCO occurs at 350 K, instead of B19 → B19′ → BCO at 400 K. Fig. 5b shows the cross-sectional view of the nanopillar in the BCO phase. Despite the apparently twinned outer boundaries, the sample is actually a single phase without twins, as evidenced by the perfect periodicity of unit cells (yellow parallelograms) in the entire system. Interestingly, it is a macroscopically twinned structure without the microscopically twinned lattice. Such type of structure arises because the orthorhombic BCO phase possesses both the mirror and central symmetries.

After the phase transformation of B19 → BCO completes, further compression causes the formation of deformation twins in BCO, resulting in a large load drop at a strain of ~6.6%. It is interesting to note that a hierarchically twinned microstructure, i.e. twins within twin, develops in the nanopillar. As shown in Fig. 5c, the boundaries of the primary twin, indicated by yellow dashed lines, are on the $\{1\,1\,2\}_{B2}$ plane, close to the orientation with the largest resolved shear stress. Within the twinning shear band, the secondary twins, indicated by black dashed lines, also develop with smaller twin widths. Such a hierarchically twinned microstructure provides an effective means of releasing strain energy, and it also enables an approximate satisfaction of geometry incompatibility across the primary twin boundaries.

During unloading, the hierarchically twinned microstructure shrinks and finally disappears, resulting in a single BCO phase without twins, i.e. recovering the structure prior to the formation of deformation twins as shown in Fig. 5b. Specifically, when the applied compressive strain is reduced from 7% to 3%, the width of the primary twin begins to decrease by migration of twin boundaries. Correspondingly, the stress–strain curve in Fig. 5a exhibits a plateau, indicating a steady-state process of boundary migration that involves a minor variation of the applied stress. At $\varepsilon \approx 3\%$, a discontinuity appears in the stress–strain curve, signifying the strain energy release caused by a complete elimination of the hierarchically twinned microstructure. No dislocation is observed in this case. After complete unloading to zero strain, the tensile residual stress remains in the nanopillar, suggesting a loss of pseudoelasticity. Since the final product is a single BCO phase without twins, the shape memory can be realized by heating or further tension, and the B2 austenite is then recovered from the BCO martensite.

Fig. 6 shows a different MD result at 350 K. Compared to Fig. 5, it also exhibits the reversible twins within twin, but pseudoelasticity rather than shape memory. The key difference between the two cases is the cross-sectional geometry of the nanopillar when the BCO phase forms during loading, i.e. the parallelogram-shaped (Fig. 6b) vs. twinned outer boundary (Fig. 5b). As a result, upon complete unloading to zero strain, the BCO phase is fully recoverable to B2, Fig. 6c; and the nanopillar has no residual stress, Fig. 6a. This is a pseudoelastic deformation.

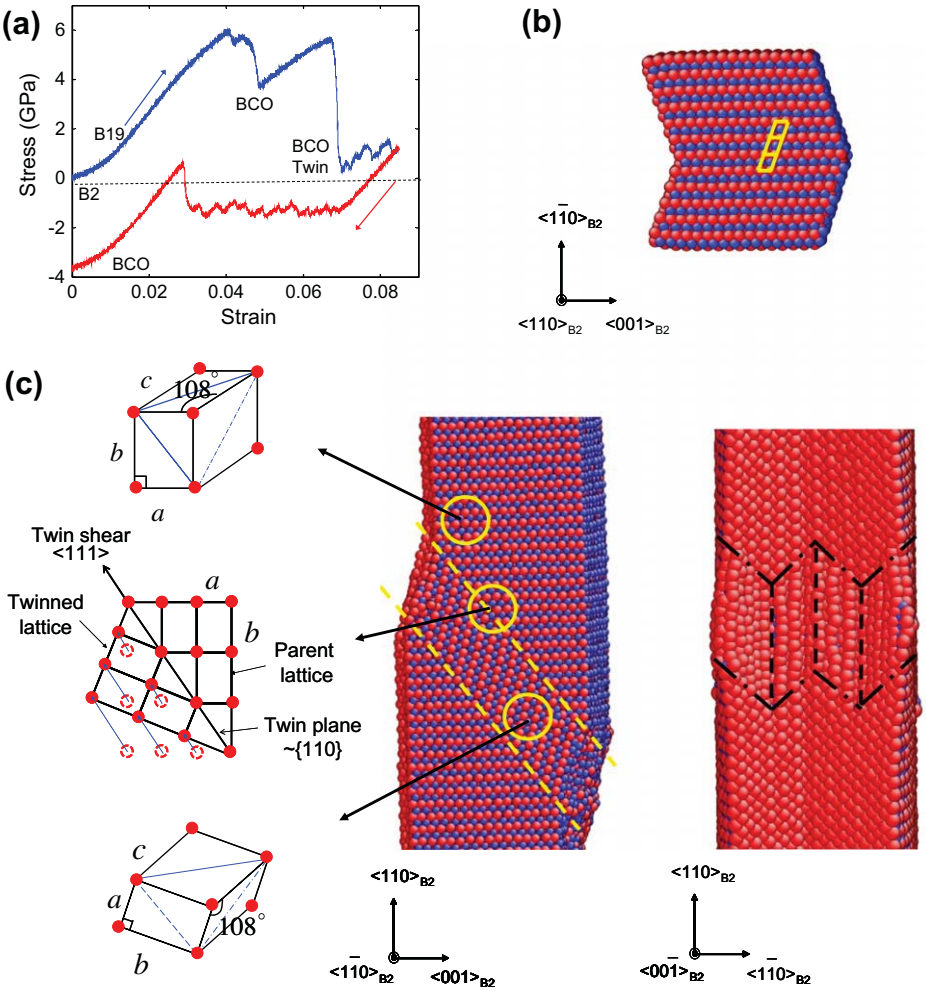

Fig. 5. Nanopillar compression at 350 K, exhibiting the shape memory behavior. (a) Stress–strain curve of loading (blue) and unloading (red). (b) Cross-sectional view of the compressed nanopillar, showing a single BCO phase (uniform unit cells in yellow lines) in the entire system despite the apparently twined outer boundary. (c) "Twins within twin" formed in a compressed nanopillar. Middle: a primary twin with twin boundaries marked by yellow dashed lines. Left: schematics of BCO unit cells of twin variants and the shear transformation at the twin boundary. Right: secondary twins (marked by black dashed lines) viewed from the $\langle 0\,0\,\bar{1}\rangle_{B2}$ direction. (For interpretation of the references to color in this figure legend, the reader is referred to the web version of this article.)

To understand the origin of the above difference in the cross-sectional geometries, we note that there are two equivalent variants that could possibly form after the phase transformation from B2 to BCO. In Figs. 5b and 6b, two BCO variants nucleate from the free surface, one at the top and another at the bottom, and they grow by migration of the respective phase boundary toward each other. If the two variants happen to be in the opposite orientation (as selected randomly by thermal fluctuations), the twinned outer boundary will eventually form, i.e. Fig. 5b. Otherwise, the parallelogram-shaped cross-section will develop, i.e. Fig. 6b. Lastly, we note a minor difference in the structure of twins within twin between Figs. 6d and 5c, while they are both reversible upon unloading.

3.4. Size effect

We have studied the size effect on the stress-driven phase transformations in NiTi nanopillars, which appears to be insignificant within the accessible size range. For instance, MD simulations at 400 K are performed as in Section 3.2, with the only difference in the doubled side lengths of the cross-section. The stress–strain curve exhibits no major change, the system similarly undergoes the phase transformations of B2 → B19 → B19′ → BCO and the deformation twinning mode is also similar. However, the twinned structure is complicated with the formation of multiple twinned shear bands, which arise due to the high symmetry of the loading orientation, as well as the large volume that promotes strain accommodation by multiple twins. As this work is focused on the unit processes of phase transformation and deformation twinning in small-sized NiTi nanostructures, it is hoped to report a detailed analysis of the spatial–temporal evolution of multi-twinned microstructures in a later paper.

Compared to the coarse-grained NiTi alloys, the nanometer size effect can be appreciated in terms of the characteristic stress–strain behaviors of NiTi nanopillars, such as

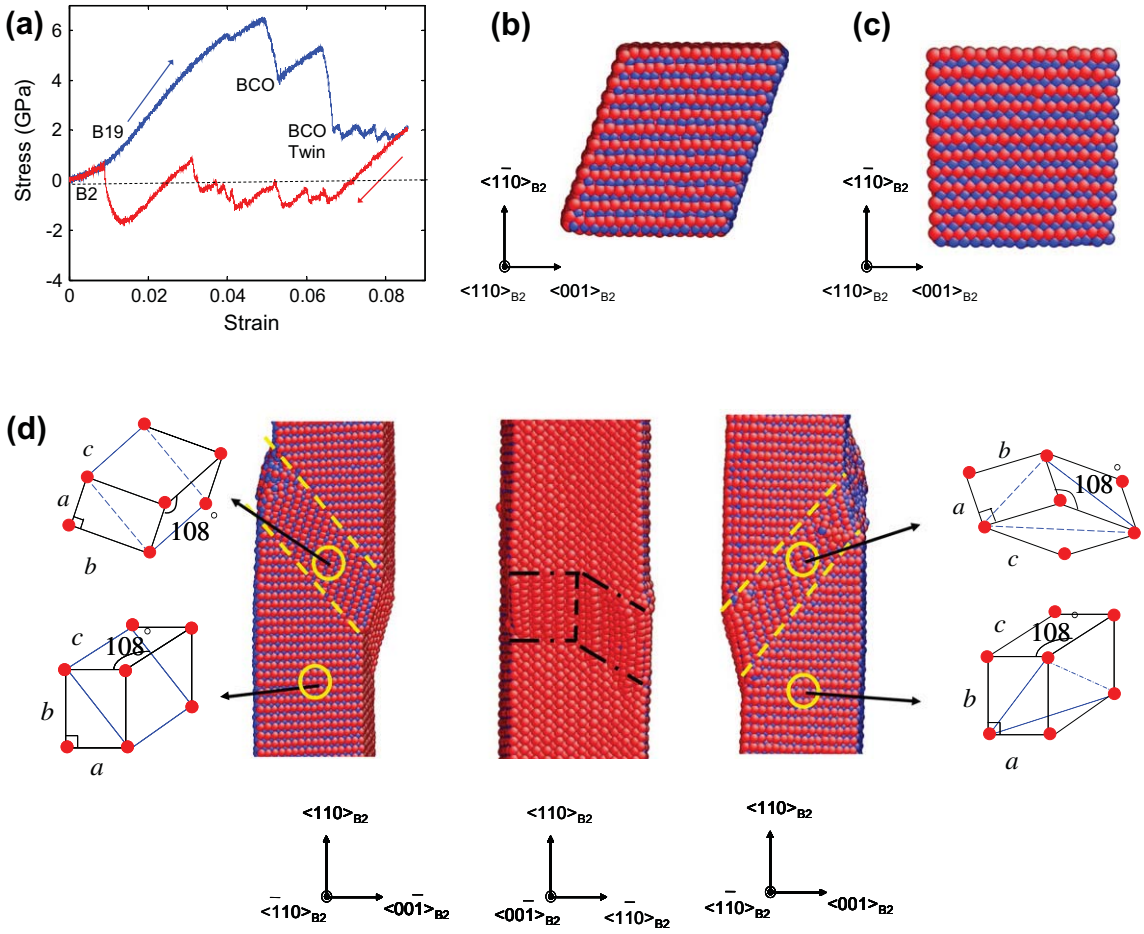

Fig. 6. Nanopillar compression at 350 K, exhibiting the pseudoelasticity. (a) Stress–strain curve of loading (blue) and unloading (red). (b) Cross-sectional view of the compressed nanopillar, showing a single BCO phase. (c) Final product of the B2 phase in a fully unloaded nanopillar. (d) A different mode of "twins within twin" formed in the nanopillar, showing three side views with the corresponding BCO unit cells of twin variants. (For interpretation of the references to color in this figure legend, the reader is referred to the web version of this article.)

the load serration, stress plateau and large hysteresis loop as revealed by MD simulations. During loading, the system has to be over-driven to accumulate a large amount of strain energy in order to overcome the nucleation barriers of phase transformation and deformation twinning in the nearly perfect nanopillar. Those nucleation processes can result in the major load drops to release strain energy, leading to serrations in the stress–strain response. During unloading, the nucleation-controlled reverse phase transformation can similarly produce discontinuities in the stress–strain curve. To understand the stress plateaus in Figs. 5a and 6a, we note that when the deformation involves the interfacial migration, the layer-by-layer movement of the twin boundaries can proceed by similar processes of atomic shuffling (as illustrated in Fig. 5c), thereby requiring a nearly constant driving stress as manifested by the stress plateau. The above considerations also allow us to rationalize the large hysteresis loop, as evident in Figs. 4–6. On the one hand, the nucleation-controlled processes during loading/unloading require the large forward/reverse transformation stresses. On the other hand, while the migration of twin boundaries during unloading is relatively easy compared to nucleation, it still requires a large load reversal, giving a low value of reverse transformation stress. This is because in nanosized systems, there is typically a lack of self-sustaining three-dimensional mechanisms (e.g. pole dislocations) to facilitate the easy movement of twin boundaries that could prevail in the coarse-grained NiTi alloys. As a result, the large hysteresis loop should feature the stress–strain curve of the nanoscale shape memory alloys, as experimentally shown in Cu–Ni–Al nanopillars [6].

In addition, we have studied the size effect on the temperature-driven martensitic phase transformation by comparing the cooling response of a bulk crystal and a nanopillar at zero stresses. In the bulk NiTi subjected to periodic boundary conditions, the martensite start temperature M_s is 310 K and the finish temperature M_f is 290 K, as shown in Fig. 2. However, in nanopillars, no phase transformation of B2 $\rightarrow$ B19′ has been observed, even when the temperature is lowered to 200 K. Such a size effect is likely related to the phase energy differences

between atoms at the free surface and in the bulk. It is noteworthy that a recent atomistic study of NiTi nanoparticles by Mutter and Nielaba [30] showed that the size effect also exists in the austenite transformation: the smaller the nanoparticle, the lower the temperatures of A_s and A_f. This trend appears to be consistent with our MD results of the lowered phase transformation temperatures with decreasing pillar size. They attributed the size effects to the increasing role of surface atoms on phase transformation with decreasing particle size [30]. This size effect on the temperature-driven martensitic phase transformation exhibits a similar trend to polycrystalline NiTi [9], where the martensitic phase transformation is suppressed when the grain size is smaller than 60 nm.

4. Conclusions

The molecular dynamics simulations of $\langle 1\,1\,0\rangle_{B2}$-oriented NiTi nanopillars have revealed the atomistic mechanisms governing the pseudoelasticity and shape memory in NiTi nanostructures. The major findings of this work are summarized as follows:

1. At high temperatures (e.g. ~50 K above the austenite finish temperature) and low loads (e.g. compressive strain up to 6.6%), pseudoelasticity dominates during the loading–unloading cycle. Imposing a higher load will result in a loss of pseudoelasticity, owing to the dislocation pinning of twin boundaries that leads to the irreversibility of deformation twinning.
2. The thermomechanical responses of NiTi nanostructures become less deterministic as the temperature decreases to around the austenite finish temperature. Both phase transformation and deformation twinning could be reversible or irreversible at high loads (e.g. compressive strain up to 10%). Only when both are reversible is pseudoelasticity realized. If only the deformation twinning is reversible, as facilitated by the formation of a hierarchically twinned microstructure, shape memory ensues.
3. The molecular dynamics results also reveal the load serration, stress plateau and large hysteresis loop in the stress–strain curves of NiTi nanopillars. These characteristics have been rationalized in terms of the nucleation-controlled phase transformation and deformation twinning, as well as the migration of phase boundaries, in nanosized volumes. It was suggested that the large hysteresis loop could be potentially utilized to provide ultrahigh mechanical damping for applications in nano/micro-devices [6].
4. Finally, we note that molecular dynamics are limited in the simulation timescale, such that they could not be quantitatively compared with experimental measurements. While some of the atomic processes revealed in this work could be specific to the model system, the mechanisms and insights concerning the reversible/irreversible phase transformation and deformation twinning should be useful for understanding the pseudoelasticity and shape memory behavior in the nanostructured shape memory alloys.

Acknowledgement

Support by the NSF Grant CMMI-0825435 is greatly acknowledged.

References

[1] Christian JW, Mahajan S. Prog Mater Sci 1995;39:1.
[2] Otsuka K, Kakeshita T. MRS Bull 2002;27:91.
[3] Otsuka K, Wayman CM. Shape memory materials. Cambridge: Cambridge University Press; 1998.
[4] Otsuka K, Ren X. Prog Mater Sci 2005;50:511.
[5] Zhu T, Li J. Prog Mater Sci 2010;55:710.
[6] Juan JS, No ML, Schuh CA. Nat Nanotechnol 2009;4:415.
[7] Krulevitch P, Lee AP, Ramsey PB, Trevino JC, Hamilton J, Northrup MA. J Microelectromech Syst 1996;5:270.
[8] Ma XG, Komvopoulos K. Appl Phys Lett 2003;83:3773.
[9] Waitz T, Kazykhanov V, Karnthaler HP. Acta Mater 2004;52:137.
[10] Waitz T, Spisak D, Hafner J, Karnthaler HP. Europhys Lett 2005;71:98.
[11] Frick CP, Orso S, Arzt E. Acta Mater 2007;55:3845.
[12] Waitz T, Antretter T, Fischer FD, Simha NK, Karnthaler HP. J Mech Phys Solids 2007;55:419.
[13] Norfleet DM, Sarosi PM, Manchiraju S, Wagner MFX, Uchic MD, Anderson PM, et al. Acta Mater 2009;57:3549.
[14] Gunderov D, Lukyanov A, Prokofiev E, Kilmametov A, Pushin V, Valiev R. Mater Sci Eng A 2009;503:75.
[15] Ye J, Mishra RK, Pelton AR, Minor AM. Acta Mater 2010;58:490.
[16] Clark BG, Gianola DS, Kraft O, Frick CP. Adv Eng Mater 2010;12:808.
[17] Simon T, Kroger A, Somsen C, Dlouhy A, Eggeler G. Acta Mater 2010;58:1850.
[18] Chen Y, Schuh CA. Acta Mater 2011;59:537.
[19] Phillips FR, Fang D, Zheng HX, Lagoudas DC. Acta Mater 2011;59:1871.
[20] Juan JMS, No ML, Schuh CA. Adv Mater 2008;20:272.
[21] Juan JS, No ML, Schuh CA. Acta Mater 2012;60:4093.
[22] Lai WS, Liu BX. J Phys – Condens Matter 2000;12:L53.
[23] Huang XY, Ackland GJ, Rabe KM. Nat Mater 2003;2:307.
[24] Wagner MFX, Windl W. Acta Mater 2008;56:6232.
[25] Hatcher N, Kontsevoi OY, Freeman AJ. Phys Rev B 2009;79:020202.
[26] Hatcher N, Kontsevoi OY, Freeman AJ. Phys Rev B 2009;80:144203.
[27] Kibey S, Sehitoglu H, Johnson DD. Acta Mater 2009;57:1624.
[28] Zhong Y, Gall K, Zhu T. J Appl Phys 2011;110:033532.
[29] Mutter D, Nielaba P. Phys Rev B 2010;82:224201.
[30] Mutter D, Nielaba P. Eur Phys J B 2011;84:109.
[31] Pun GPP, Mishin Y. J Phys – Condens Matter 2010;22:395403.
[32] Holec D, Friák M, Dlouhý A, Neugebauer J. Phys Rev B 2011;84:224119.
[33] Park HS, Gall K, Zimmerman JA. Phys Rev Lett 2005;95:255504.
[34] Liang WW, Zhou M, Ke FJ. Nano Lett 2005;5:2039.
[35] Li SZ, Ding XD, Deng JK, Lookman T, Li J, Ren XB, et al. Phys Rev B 2010;82:205435.
[36] Li SZ, Ding XD, Li J, Ren XB, Sun J, Ma E, et al. Phys Rev B 2010;81:245433.
[37] Finnis MW, Sinclair JE. Philos Mag A – Phys Condens Matter Struct Defects Mech Prop 1984;50:45.
[38] Plimpton S. J Comput Phys 1995;117:1.
[39] Brill TM, Mittelbach S, Assmus W, Mullner M, Luthi B. J Phys – Condens Matter 1991;3:9621.
[40] Otsuka K, Ren X. Mater Sci Eng A 1999;273:89.

[41] Qiu S, Clausen B, II SAP, Noebe RD, Vaidyanathan R. Acta Materialia 2011;59:5055.
[42] Ishida A, Sato M. Acta Mater 2003;51:5571.
[43] Fu YQ, Zhang S, Wu MJ, Huang WM, Du HJ, Luo JK, et al. Thin Solid Films 2006;515:80.
[44] Juan JS, No ML, Schuh CA. J Mater Res 2011;26:2461.